# Stress determination in a thermally grown oxide on Ni38Cr alloy by use of micro/nanogauge gratings

Benoît Panicaud, Abdelhamid Hmima, Cécile Rampelberg, Mbaye Ngom, Florimonde Lebel, Guillaume Geandier, Thomas Maurer, Jean-Luc Grosseau-Poussard, Emmanuel Guyot, Jérémie Béal, et al.

Version of Record: https://www.sciencedirect.com/science/article/pii/S0921509321003488
Manuscript_5569d437de880141c15985e4b64697e9

# Stress determination in a thermally grown oxide on Ni38Cr alloy by use of micro/nanogauge gratings.

Benoît Panicaud[a,*], Abdelhamid Hmima[a], Cécile Rampelberg[b], Mbaye Ngom[a], Florimonde Lebel[b], Guillaume Geandier[b], Thomas Maurer[c], Jean-Luc Grosseau-Poussard[d], Emmanuel Guyot[a], Jérémie Béal[c], Joseph Marae-Djouda[e], Léa Le Joncour[a], Akram Alhussein[f]

[a]*Life Assessment of Structures, Materials, mechanics and Integrated Systems (LASMIS); Université de Technologie de Troyes (UTT); 12, rue Marie Curie - CS 42060 - 10004 Troyes cedex - France*
[b]*Institut Jean Lamour (IJL) CNRS UMR 7198; Université de Lorraine; Campus ARTEM, 2 Allée André Guinier - BP 50840 - 54011 Nancy Cedex - France*
[c]*Light, Nanomaterials, Nanotechnologies (L2n) CNRS ERL 7004; Université de Technologie de Troyes (UTT); 12, rue Marie Curie - CS 42060 - 10004 Troyes cedex - France*
[d]*Laboratoire des Sciences de l'Ingénieur pour l'Environnement (LaSIE) CNRS UMR 7356; Université de La Rochelle; Avenue Michel Crépeau - 17042 La Rochelle Cedex 1 - France*
[e]*ERMESS, EPF, Ecole d'ingénieur-e-s; 3 bis rue Lakanal - 92330 Sceaux - France*
[f]*Life Assessment of Structures, Materials, mechanics and Integrated Systems (LASMIS); Université de Technologie de Troyes (UTT); Pôle Technologique Sud Champagne, 26 Rue Lavoisier - 52800 Nogent - France*

## Abstract

Residual stresses in thermal oxide layer may be significant and can influence the lifetime of systems in high temperature environments. It is thus relevant to determine locally stress and strain mechanisms and especially the mechanical relation between the oxide layer and the metallic substrate. To achieve such a goal, an innovative approach is proposed by use of micro/nanogratings. Monitoring experimentally the gauges displacement during high temperature oxidation and considering a specific model, we are able to determine thermomechanical quantities both in oxide $Cr_2O_3$ and in metallic alloy Ni38Cr, as well as their evolution during the oxidation time. Parameters values for calculations of the stress versus time evolution are also provided.

*corresponding author benoit.panicaud@utt.fr

*Keywords:* high temperature behavior, growth stress determination, microgauges, local strain, 2D mapping, short oxidation times

## 1. Introduction

The presence of residual stresses in thermal oxide layers has been recognized for a long time [1, 2, 3]. In particular, the growth stresses occurring during isothermal oxidation process may influence the protective properties of the oxide scales, by reducing the lifetime of the metallic substrate. Irrespective of the particular alloy being oxidized or the kind of oxide formed, the growing oxide film is usually under significant stresses (around GPa). Thus, it is important to accurately determine the strain and stress fields associated to the growth of oxide films on metallic substrates to investigate the lifetime of such systems. On one hand, the determination of residual stresses of oxidized materials was often already performed experimentally after cooling, thus requiring the subsequent determination of both thermal and/or growth stresses by calculations [4, 5]. On the other hand, the in-situ experimental determination of oxide stresses is less common because more difficult. Indeed, it is important to investigate in-situ systems for both isothermal and non-isothermal conditions and study the associated mechanisms (growth and relaxation).

In thermal growing oxide, stress is varying along the time under isothermal or non-isothermal conditions. This stress is related to different origins (growth, thermal mismatch, dissolution in the metal, epitaxy...) that are mostly related to geometrical incompatibilities [3]. Consequently, it can lead to effects of relaxation depending on different conditions in the oxide (for example grain size) that can damage or not the oxide scale (creep, cracking, debonding, buckling, rumpling...) [1]. The damage mechanisms have an influence on the lifetime of the system, and may play a significant role with a possible acceleration of the oxidation by breakaways phenomena [2]. By determining the time evolution of stresses, it is possible to identify specific phenomena that would influence this lifetime.

One aim of the present study is to propose an original technique to map strain and stress in all the systems phases, and especially in the oxide layer, obtained from in-situ determination during high temperature oxidation. The main idea consists in fabricating micro or nanoparticles gratings with micronic or submicronic distances in order to track displacements and then

map different fields (strain, distortion, stress...), as described in [6, 7, 8]. Particles thus play the role of gauges. To achieve such a goal, gratings are fabricated using electron beam lithography (EBL). It was successfully applied to metallic alloys stainless steel (306L, UR45N) and titanium. In this article, we are exposing the principle of this technique applied in the context of high temperature oxidation. We have applied it to Ni38Cr alloy specimen to map the evolution of local strain and stress, in the growing oxide layer as well as in the metallic alloy, as a function of the oxidation time. Such a methodology is similar to the one proposed in the work of A. Clair [9]. The present work aim at obtaining more quantitative results to confront experiments and modelling. Data treatment of the information obtained by in-situ microscopy is required, as well as specific modelling of the thermomechanical behavior. Similarly to the use of nano-particles on metallic alloys as described in [6, 7, 8], we expect to know whether the local heterogeneities of the oxide microstructure may be followed, in the case of oxide growing on Ni38Cr at $800^oC$ corresponding to a common use in manufacture industries.

In the present article, we are first describing materials and experimental characterization of these materials. The next sections deal with the different steps of the process: fabrication of gratings, in-situ following by confocal microscopy, identification of the gauge centers, and data treatments based on specific assumptions. The last section will illustrate the use of the method to obtain results on the studied system.

## 2. Materials

### *2.1. Description of the metallic alloy*

In the present article, a chromium content substrate is considered, especially the alloy Ni38Cr. The latter is an oxidation resistant chromia-forming alloy whose oxidation behavior has been extensively studied because of its industrial applications [10, 11, 12, 13]. The shape of the samples used for preliminary characterizations is a cylinder of radius 6mm and thickness 4mm. The substrate material is a NiCr alloy that should contain an atomic percentage of 38% Cr, corresponding to a mass percentage of 35% Cr. We have checked this composition by use of EDS analysis. The chemical composition (normalized mass percentages) is measured at 64.94% for Ni and 34.15% for Cr, on the surfaces further submitted to oxidation, close to the expected value.

Concerning this substrate, the samples have been first heat treated to stabilize the grain size. They were heated during 1 hour at $1000^oC$, then polished before new oxidation. Using these samples further at $800^oC$ should not lead to an evolution of the substrate grain size. Moreover, we have controlled by observations that during oxidation from $25^oC$ to $800^oC$ the grain sizes of the surface do not evolve.

Metallographic analysis has also been performed with chemical treatment HCl 95% $+ H_2O_2$ 5% during 20s. The corresponding picture can be seen in Fig. 1. We have analyzed the metal composed of equiaxed grains of Ni phase. There is no precipitate neither intergranular phase.

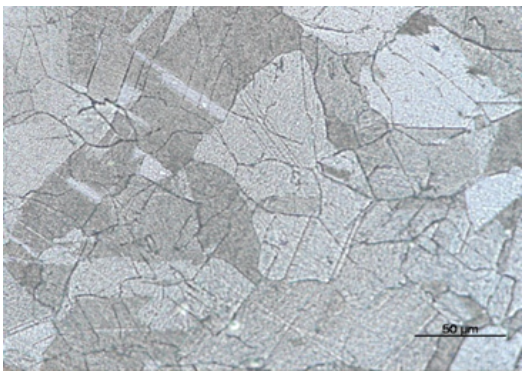


Figure 1: Chemical treatment on the surface of Ni38Cr.

EBSD analysis has also been performed to check the texture of the substrate, by use of FEI-Quanta-650-FEG (20kV-3nA). The area of the EBSD mapping is $1306.8\text{m} \times 899.1\text{m}$ with a step of 2.7m. The acquisition has been performed with HKL channel5 (Oxford Instrument). Post-treatment with Tango software and the indexation rate before cleaning is 81.34%. It leads to the Inverse Pole Figure (IPF) maps presented in Fig. 2. EBSD analysis has proved that for all the directions, there is no specific texture on this material. It enables also to give a grain size distribution whose statistical average over 1507 grains is $24.9 \pm 14\text{m}$, which corresponds to a value similar to previous works with the same material [14]. Grain size has been measured using the standard intercept method. Twins are considered as different grains. The range of the grain size in the analyzed area is between 11.2 and 109.3m. Grain with a size smaller than 11m has been removed.

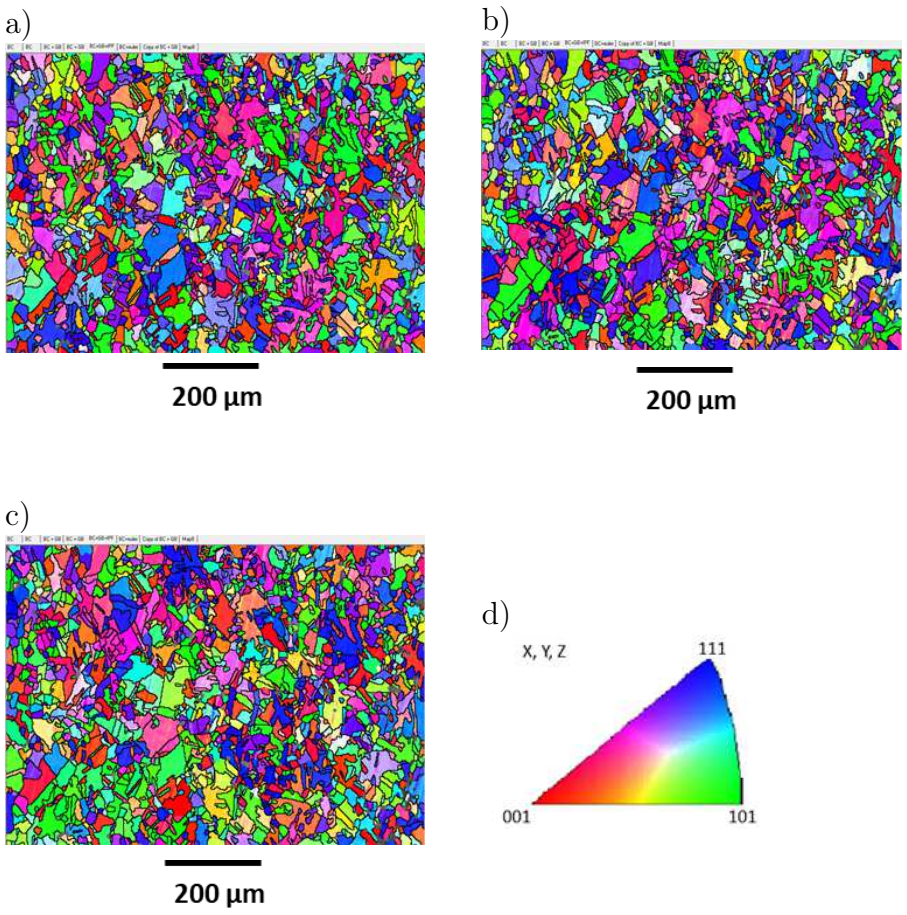


Figure 2: IPF maps of Ni38Cr. a) X direction; b) Y direction; c) Z direction d) standard unit triangle ; Colors correspond to the crystallographic orientations according to the standard unit triangle; as there is no texture, RD, TD and ND are equivalent.

### *2.2. Description of the oxide layer*

This kind of material is an oxidation-resistant chromia-forming alloy and its oxidation behavior has been largely studied. Indeed, this alloy is attractive for fundamental investigations because the oxide formed is mainly chromia $Cr_2O_3$ for the investigated temperature of $800^oC$ and for the considered partial pressure (see below). Hence the complexity associated with competitive growth of different oxides, such that occurring during the oxidation of alloys, is avoided [15]. Different temperatures from $700^oC$ to $900^oC$ were deeply

studied in [16]. This system had been also compared with the results proposed by Mougin [17], who also considers the same oxide but growing on a different substrate.

We have presently tested the oxidation at 800$^o$C with a laser confocal microscope (LSM700 - ZEISS). It is equipped with a high temperature stage (TS1500 - Linkam) that enables to do in-situ measurement. Thermal loading has been chosen with a heating rate at 150$^o$C/min followed by a plateau of 3h and then a cooling rate of 200$^o$C/min. For the presented results at 800$^o$C, the Ar flow is $3l/h$ corresponding to a partial pressure of $3 \cdot 10^{-4}$atm. An EDS analysis has been performed on the cross-section of samples oxidized following the previous thermal loading. An illustration is shown in Fig. 3 for 800$^o$C. We can see that Ni remains in the substrate. Cr is present in the oxide layer certainly through a diffusion mechanism. In the studied range of temperature, it is admitted that cationic diffusion mainly occurs with outward oxidation [18]. A Cr depletion zone can be observed at the metal-oxide interface (around 1m depth in the near interface). Oxygen remains only in the oxide layer and no dissolution of anion is observed in the present substrate.

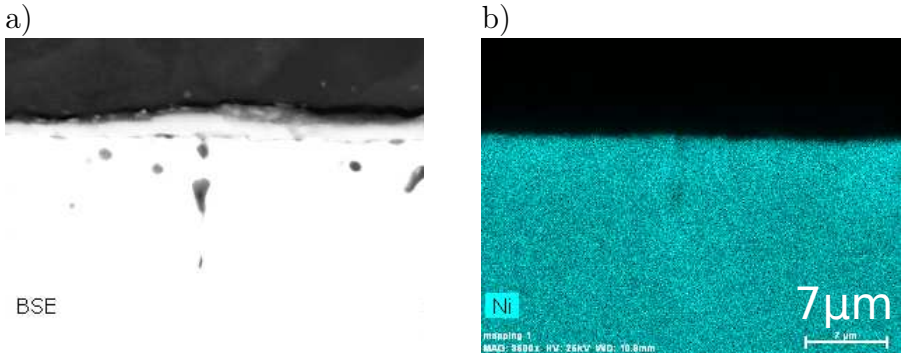


From these cross-sections, we have also measured the oxide layer thickness by use of BSE detector on SEM images. For 800$^o$C during 3h with the high temperature stage, the observed averaged thickness is 258.4nm $\pm$ 104nm. Previous works on the similar system [14] give oxidation kinetics constant for parabolic regime of $A_{\mathrm{p}} = \sqrt{k_{CP}} = 2.36 \cdot 10^{-9}\mathrm{m} \cdot \mathrm{s}^{-1}$ at 800$^o$C. For 3h at this temperature, it leads to 245nm, assuming homogeneity of the layer, that is of the same order of magnitude than the measurements from our cross-sections.

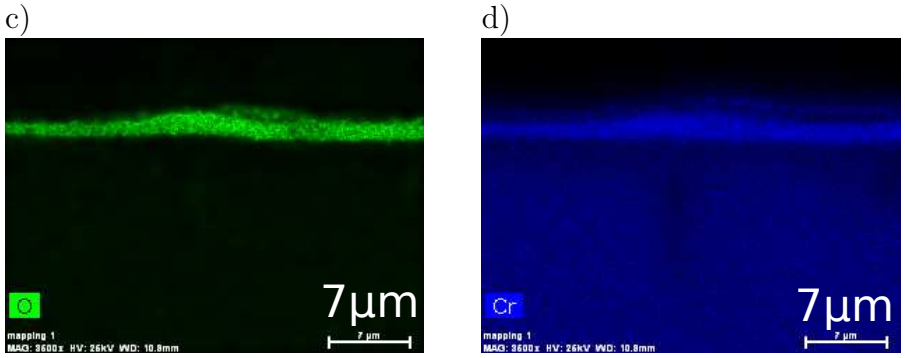


Figure 3: Chemical analysis of the cross-section of oxidized Ni38Cr for oxidation at $800^oC$ during 3h: a) BSE cross-section; b) Ni content; c) O content; d) Cr content ; ellipse in red is the location of Cr depletion.

We have also performed XRD analyzes to identify the phases. Such an identification has been performed with a Bruker D8 discover on a Bragg-Brentano diffractometer with a Cobalt source at $\lambda = 1.78897A$ equipped with a 4-circles goniometer and Linx-eye detector. In the range of the studied temperatures during 3h, we have clearly identified the FCC phase of Ni as well as rhombohedral $Cr_2O_3$ that are the only detected phases. This is in good agreement with the different studies in NiCr alloys [14, 15, 18, 19, 20]. Diffractograms are not presented in the article but one example is provided in the supplementary material.

## 3. Studying process for thermomechanical characterization

In the present study, we aim at following the displacement of gratings during the oxidation to obtain the thermomechanical state and its evolution in the different materials of the system. In the present work, we propose a method based on 4 steps:

- First, we make periodic gratings with initial circular particles by use of electron beam lithography;
- Second, we make in-situ following of this gratings by confocal microscopy;
- Third, we try to identify the centers of the particles of the gratings;

- Fourth, we make different data post-treatment to obtain the strain of particles, as well as other mechanical quantities in the different phases.

### *3.1. Fabrication of periodic gratings*

#### *3.1.1. Electron beam lithography (EBL)*

Specific material can be deposited on top of the specimen using EBL over a zone as large as 100m to 1000m Their height is set around few hundreds of nm while the inter-particles distance is kept constant. Precautions have been taken to guarantee that the gratings main axes are parallel to the main axes of the metal alloy specimen. The specimen was polished before the deposition of the particles gratings. For the polishing, several grain size papers (600, 800, 1200, 2500) were used, up to a 1m particle solution. All the samples were cleaned with acetone in ultrasonic bath. However, the approach can be applied without any significant surface preparation. It is only important to have a surface roughness small enough compared to the size of particles. The idea is to provide a surface roughness to the samples that cannot affect the electron beam lithography, as well as to obtain a pattern of cylindrical nanogauges all in the same direction at initial step. Consequently, attention should be taken in the lithography process: the thickness of the resin is not uniform and if surface is not smooth, it leads to the defocusing of the electron beam during the patterning and difficulties during the lift-off process. In fact, the metal film does not peel off the surface. Important roughness could also introduce some artefacts in the imaging of the surface. Indeed, the focus is harder to achieve for a surface with a great topography gradient. The main steps of the process of lithography are shown in Fig. 4. For the choice of the deposited material, specific constraints have to be taken into account. Mainly, in the context of high temperature oxidation, particles should resist to a maximum temperature at $800^o$C. Tests have been performed with different metals: Au, Pd, Pt, Ti, up to $900^o$C. Other materials have been tested and will be presented in a further communication. For room temperature application, gratings of Au particles are usually considered [6, 7, 8]. However as illustrated in Fig. 5, Au is not able to resist in the range of the studied temperatures for the oxidation time. Indeed, we can observe a change of the shape at $900^o$C that does not allowed further correct identification of particles center. Similar conclusions can be drawn for Pd and Pt (see in Fig. 6 and Fig. 7), either because it does not mechanically holds at high temperature, or because of a bad contrast with the oxidized substrate that would limit the efficiency of the identification step.

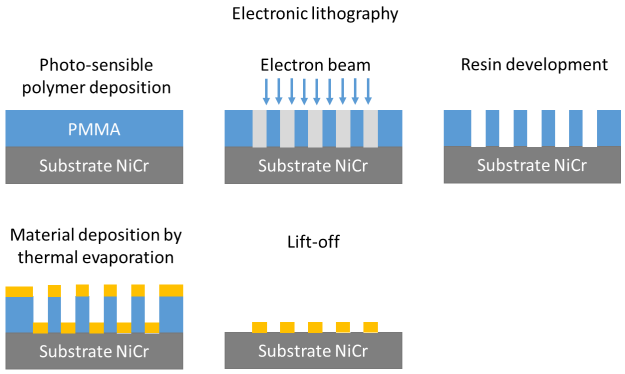


Figure 4: Gratings fabrication process by use of EBL

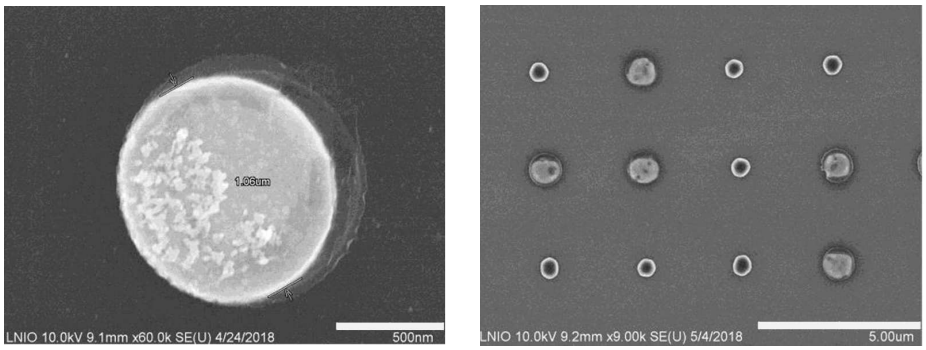


Figure 5: Evolution of Au particle at 900$^o$C during 30min in an inert environment (no oxidation occurs); left at room temperature (initial surface shape is a circle); right at 900$^o$C after 30min

At the contrary, Ti is able to resist in such a range of temperature. Oxidation may also occur in the surface of particles (see in Fig. 8 at the right). However the shape is stable during the oxidation time at the considered temperature. Moreover, the contrast remains sufficient for further distinction with the oxidized substrate to get a correct identification.

Another problem comes from the choice of the particles geometry. Even if different shapes have been tested (circle, square), we choose to use circular ones. It was demonstrated as quite efficient for further identification of their position by use of the developed data treatment [6, 7, 8]. We just have now to define a correct height and radius for the particles.

The radius should be chosen as small as possible. Typically, we except

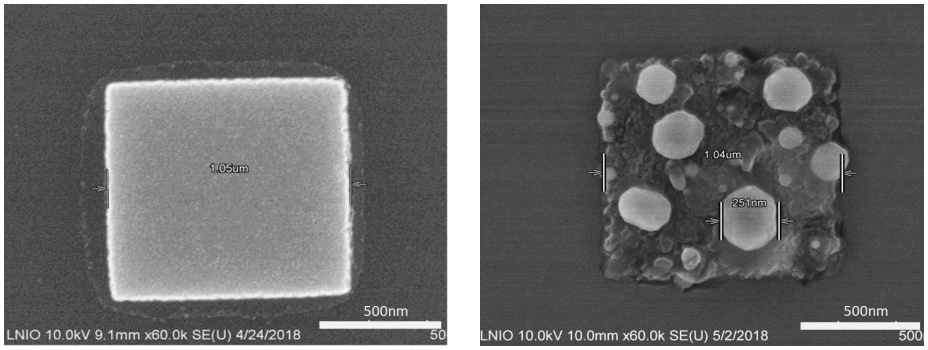


Figure 6: Evolution of Pd particle at 900$^o$C during 30min in an inert environment (no oxidation occurs); left at room temperature (initial surface shape is a square); right at 900$^o$C after 30min

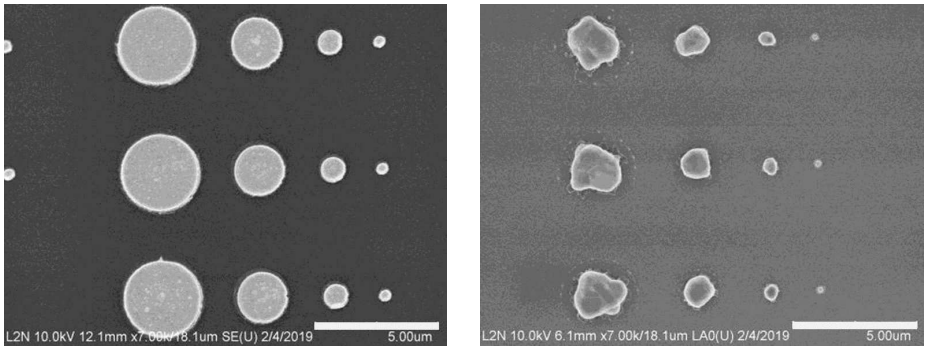


Figure 7: Evolution of Pt particle at 900$^o$C during 30min in an inert environment (no oxidation occurs); left at room temperature (initial surface shape is a circle); right at 900$^o$C after 30min

particles that do not perturb the measurement. Moreover, smaller are the particles, better is the spatial resolution of the method. This aspect was investigated in previous studies with nanogauges [6, 7, 8].

However, there are several strong constraints for fabrication and use of these particles for the concerned application:

- Particles has to be as high as possible to limit the oxide covering. Indeed, as previously written, the thickness of the oxide layer is around 250nm at 800$^o$C during 3h. It means that at least micronic particles or slightly inferior would be better considering the chosen temperature;

- During the fabrication, to avoid conic shape by shadowing effects (as presented in Fig. 9), the higher or larger are the particles, the better it

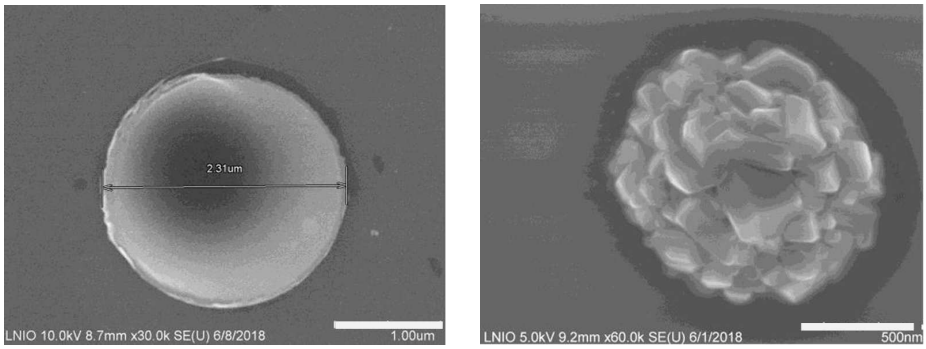


Figure 8: Evolution of Ti particle at $900^o$C during 30min in an oxidant environment (oxidation occurs); left at room temperature (initial surface shape is a circle); right at $900^o$C after 30min

is with fixed conditions of PMMA deposition (polymethyl methacrylate is widely used with electron beam process) ;

- Fabrication of high particles takes however very long time: common gratings are generally limited to a height inferior to 1m;
- High particles needs to have a large radius (a ratio of three is generally used during EBL). This ratio ensures mechanical stability. Indeed, natural bending or bucking of the particles may occur during their further use if this condition is not fulfilled;
- During identification step of the particles center, precision of the method is better for a large radius with enough pixels (for a given size of these pixels). It increases the method accuracy.

As a consequence, a compromise has to be found. For their use at $800^o$C, we have obtained micrometric particles for their diameter (3m) and nanometric for their height (300nm) made of Ti. The particles are thus both micrometric and nanometric. We have performed fabrication of gratings of 140m $\times$ 140m with 25 particles per row and 25 particles per column (total of 625 particles deposited on the surface). The distance between 2 particles (center to center) is thus around 5.8m.

The conical shape of the gauges is not a problem for the detection of the centers since the symmetry is respected during the oxidation, but what can pose a problem is to pass to slightly straight flanks (angle of the vortex of the cone greater than $20^o$). The growth of the oxide (vertical and horizontal)

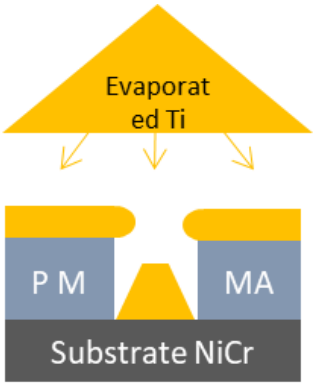


Figure 9: Magnification of the material deposition step

around the cone is not slowed down and the oxide covers the gauge faster than if its sides are straight (cylindrical gauge). In the case of this article, the height of the plots of $300nm$ gives an angle of $85^o$, which leads to a horizontal acceleration of growth much more visible with small diameters (less than 1m).

The gratings at room temperature and at the final time of oxidation at $800^o$C are presented in Fig. 10. It can be observed that the quality of the picture is not the same due to the oxidation effect and that the data treatment should be able to deal with such differences of contrast. For a given picture, we can see difference of contrast from a spatial part to another with high heterogeneity. However, almost all particles remain visible and can be distinguished that validates the condition of the fabrication step. Even if the thickness of the oxide layer is of the same order than the particle height (300 nm), there is no significant covering.

*3.1.2. In-situ microscopy during high-temperature oxidation*

In this present work, in-situ observations of formation and growth of oxide films at high operating temperature were performed with a laser confocal microscope (LSM700 - ZEISS) equipped with a high temperature stage (TS1500 - Linkam). This stage allows microscopy in the temperature range from room temperature to $1500^o$C. The principle of the laser scanning confocal microscope is to focus, via an objective lens, a laser beam (wavelength of 405nm), which illuminates a point of the sample, then to focus, on a detector, the light signal reflected at this point via a beam splitter. By scanning

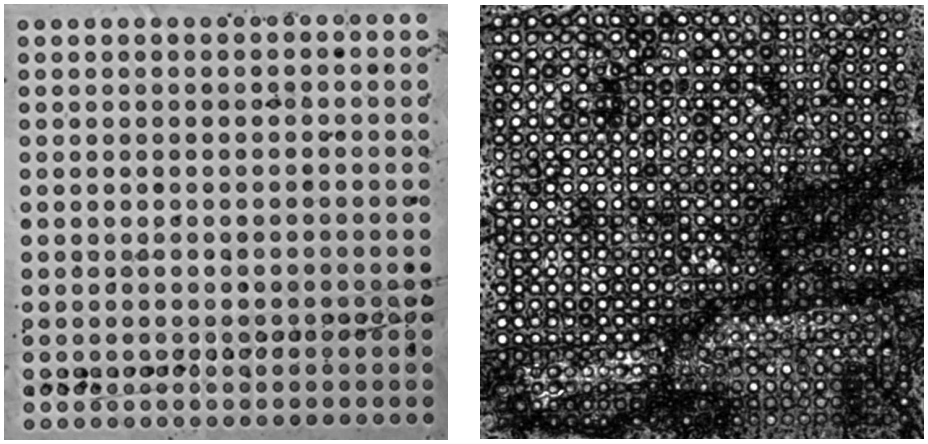

Figure 10: Gratings of Ti particles; left at $100^o$C, which is almost similar to room temperature micrography (not presented here); right at $800^o$C after 3h. Pattern is systematically a square of 150m*150m of 25*25 nanogauges of $6\mu m$ intergauges distance center to center

the focused spot relative to the object, a picture can be constructed point by point. This technique operates with a confocal pinhole, only light emitted in the focal plane can reach the photodetector; the light from out-of-focus plans is blocked by this system. As a result, a thin optical section is created, providing a picture with increased resolution compared to equivalent light microscopes. The pinhole placed in front of the photodetector also blocks the thermal radiation emitted from the heated specimen other than the focal plane. Hence, it is possible to observe sample at high lateral resolution at elevated temperature. Thus, this technique is ideally suited for in-situ study of high temperature processes. Specimens are placed inside an alumina crucible beneath a quartz view port. The heating element is a coiled platinum wire around the ceramic crucible. Specimens are heated from underneath as well as from sides. To measure the temperature, a S-type thermocouple is fixed on the bottom of the crucible, close to the sample. During the heat treatment, pictures are recorded continuously at a frame per 1.56s and stored with resolution of $1024 \times 1024$ pixels. Sample for laser confocal microscope was specifically machined into a 6mm square and 350m thick and then polished conventionally to a mirror finish (according to the description in section 3.1.1). Features of the microscopy observations are summarized in Table 1. The heating process was as follows: the specimen was heated until $800^o$C at a heating rate of $150^o$C/min and held for 180min $= 3$h and then cooled to room temperature, as presented in Fig. 11.

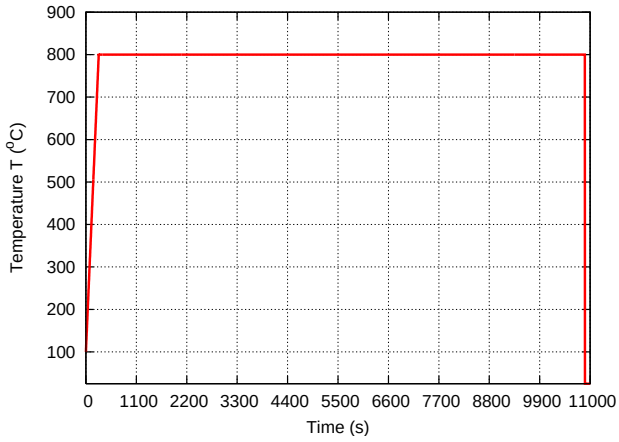


Figure 11: Temperature loading (temperature has been initially measured from 100$^o$C)

| | |
|---|---|
| Focal lens | $\times$20 |
| Picture zoom | 1.4 |
| Picture size | 228.4m $\times$ 228.4m |
| Resolution | 1024 $\times$ 1024 |
| Pixel size | 0.223m |
| Scan speed | 1 picture per 1.56s |

Table 1: Features of the microscopy observations

During the microscopy at high temperature, with the chosen scan speed, we have obtained 7009 pictures that require the use of an automatic algorithm to identify the 625 particles per picture.

### *3.2. Data treatment*

#### *3.2.1. Particles displacement and displacement gradient tensor*

First step of the data treatment corresponds to the identification of the particles center. It has been performed by use of a homemade software programmed with Matlab. Input data are required, such as the numbers of rows and columns of the gratings. It is provided with the first picture. Then on all the next pictures, we require to have the same number of particles per column and per row, as well as a correct ordering for further comparisons

between pictures. The respect of a well indexation of the particles for all the micrography pictures is indeed the crucial feature guaranteeing the computation of kinematic fields. To be sure that the particles are well indexed from 1 to 625, they are displayed in the screen to check.

The algorithm first uses automatically the Hough transform to identify positions (x and $y$ coordinates to the origin of the pictures placed at the top left of each picture) [21]. Features of the Hough transform requires to provides four parameters to optimize the identification: tolerance and sensibility parameters, as well as the range of radii (min and max), in which we expect to find the particles. The radius of all the particles is therefore obtained, as well as their positions and then saved as a vector in a data file. Because pictures may have defects (see for example in Fig. 10 on the right), there is sometimes difficulties for the Hough transform that requires either to add manually particles or to remove positive false. For a given set of parameters, the particles center identification is finished when the $25 \times 25$ particles are all treated. Then the algorithm passes to the next picture, with a correlation function to help to find more easily the moved particles. It improves the efficiency of the Hough transform. This step is repeated then for all the pictures. To spare time, we have skip pictures and we are presenting the results only for 523 pictures during the oxidation time (except for the cooling part because we are presently interested for short times or isothermal results). The critical point in the picture analysis may occur for large strain values when large distortions of the gratings may induce large local displacements of the particles, which thus make confuse the particles indexing. This aspect is presently avoided because strains in oxide, substrate or particles remains at small deformation (typically above $1.3 \cdot 10^{-2}$ that is very small to unity).

For all the calculated kinematic fields, the reference was taken at the initial state without loading. The displacement of particles are therefore calculated by comparison between a picture $k$ at time $t$ with this initial picture. Any rigid body motion of the systems have been removed by superposition of the origins of the two compared pictures. The equation to calculate the particles displacement (particle $i$ of center of gravity with coordinates $(x_i, y_i)$ on the 2D surface) is as follow:

$$u_x^k(x_i, y_i) = x_i^k - x_i^0 \quad (1)$$

$$u_y^k(x_i, y_i) = y_i^k - y_i^0 \quad (2)$$

From the particles radius and displacement, we can now obtain different

quantities. From the first one, we can calculate the perimeter, the area or the circularity of the particles. From the second one, we can calculate different kinematic fields, as already proposed in [6, 7, 8]. However, the high temperature oxidation leads to specific assumptions to obtain the different quantities:

- Chromium oxide does not grow at the interface Ti/substrate with adherence/contact of the particles on substrate; acccording to the observations, it has been controlled that all the gauges remain adhesive to the substrate at $800^o$C during all the oxidation duration ; the influence of this assumption will be discussed in section 5;

- Particles remain cylinders with elliptic basis; the circularity is not required, but for simplicity and according to the obtained pictures, it is also assumed with a good confidence (see Fig. 10 on the right);

- Particle strain is considered as the same as the strain derived from its neighbors, leading to finite strain calculation by the displacement of its neighbors (Eulerian finite transformation is considered as a generality even if the strain is small; this aspect has been checked by calculations of different strain expressions that do not present significant differences);

- The out-plane components of the displacement gradient tensor $H_{zx}$ and $H_{zy}$ of particles are negligible for calculation of the in-plane strain components, meaning that we consider a 2D calculation. With the present assumption, even not strictly equal to zero, those terms are expected small and their products, as quadratic terms, are weak compared to linear terms, because the loading leads to a response in small deformation as previously written.

The last three assumptions are not specific to the high temperature oxidation, but are generally and successfully used for such a method [6, 7, 8].

Once the displacement field is obtained for each particle of the gratings, finite deformation formalism enables to calculate others kinematics fields. Calculations are made to the deformed configuration (at each loading step which are finite) so that the use of finite deformation is required [22]. The displacement gradient second-rank tensor field $H_{jl}(x_i, y_i)$ is locally calculated for each particle by using the neighboring particles by use of derivative

formulas. $j, l$ are lowerscripts equals to $x$ or $y$. Homemade software was implemented for calculations and analyzes. The software gives the possibility to use three or five neighboring particles for the derivative calculations (see Fig. 12 for the presently used case), in function of which formulation gives the best description of the strain of the material surface (with the less derivative noise).

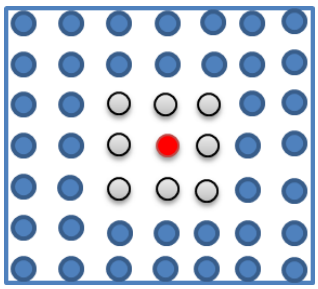

Figure 12: Derivative scheme using 3 points in $x$ direction around/including the (red) particle, for which a kinematic quantity is calculated; the same is considered in the $y$ direction

In the case of a 3 points centered derivative scheme, the displacement second-rank gradient tensor $H_{jl}$ is calculated as:

$$H^k_{xx}(x_i, y_i) = \frac{\partial u^k_x(x_i, y_i)}{\partial x_i} \approx \frac{u^k_x(x_i + \Delta x, y_i) - u^k_x(x_i - \Delta x, y_i)}{2\Delta x} \quad (3)$$

$$H^k_{xy}(x_i, y_i) = \frac{\partial u^k_x(x_i, y_i)}{\partial y_i} \approx \frac{u^k_x(x_i, y_i + \Delta y) - u^k_x(x_i, y_i - \Delta y)}{2\Delta y} \quad (4)$$

$$H^k_{yy}(x_i, y_i) = \frac{\partial u^k_y(x_i, y_i)}{\partial y_i} \approx \frac{u^k_y(x_i, y_i + \Delta y) - u^k_y(x_i, y_i - \Delta y)}{2\Delta y} \quad (5)$$

$$H^k_{yx}(x_i, y_i) = \frac{\partial u^k_y(x_i, y_i)}{\partial x_i} \approx \frac{u^k_y(x_i + \Delta x, y_i) - u^k_y(x_i - \Delta x, y_i)}{2\Delta x} \quad (6)$$

where $\Delta x$ and $\Delta y$ are the steps in direction $x$ and y, respectively. It is worth noting that in the present case, $\Delta x = \Delta y$. The gradient tensor $H_{jl}$ represents a gradient relative to the Eulerian positions. The Euler-Almansi strain tensor field $\varepsilon^k(x_i, y_i)$ for image $k$ can be deduced from this displacement gradient tensor and the strain maps can be computed (detailed equations can be found in [6, 7, 8]). It is important to note that this displacement gradient $H_{jl}$ is

evaluated using the actual coordinates. This is not usual but corresponds to the information that we can directly obtain from the experiments. It means that the calculation is performed in finite deformation and is naturally Eulerian. The use of this tensor also enables the calculation of other in-plane kinematic quantities: distortion...

### *3.2.2. Modelling of the thermomechanical behavior of oxide and metal with $N \times N$ particles*

From the particles gratings displacement, we want now to obtain other stress and strain tensors, especially in oxide layer and metallic substrate. We need therefore to relate it to the thermomechanical behavior of the system. A modelling of the system is thus required. The considered geometry configuration is given in Fig. 13.

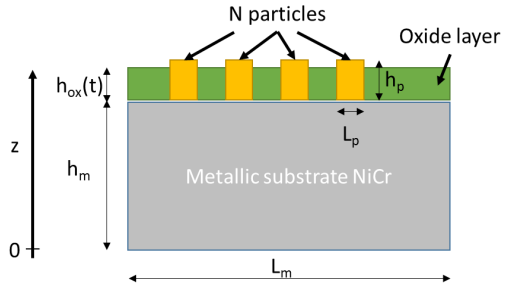


Figure 13: Geometric configuration of the thermomechanical problem

The main following assumptions are presently made (in addition to those in previous section):

- Mechanical kinematics is eventually considered for small deformation because of the previous experimental observations for strain values;
- The average stress may be calculated without taking into account the existence of a possible stress gradient;
- The force balance equation for static conditions is used by considering in-plane stress;
- The positions of the interfaces and z coordinate are defined in Fig. 13, by reference to a median line. The subscripts "ox" and "m" refer respectively to oxide and metal;

- The system has an isotropic and biaxial behavior (stress state); because of some symmetries of the problem, it leads to assume a 2D problem in plane $(x, z)$ or $(y, z)$, for which we will be able to test experimentally the hypothesis;
- Some two-dimensional mechanical effects such as rumpling are not considered;
- The non-linear mechanical phenomena (buckling, cracking, spalling) are not considered;
- Therefore, for all time, there is always displacement continuity at the oxide/metal interface;
- Temperature may evolve with time, but no space gradient of temperature is considered;
- Only one single phased oxide layer is considered on the metal and this phase is time-independent (no chemical transformation are considered within the bulk of the oxide, except the oxidation itself).
- It is a priori necessary to distinguish two possible cases: symmetrical oxidation (when the two metallic sides are oxidized) and asymmetric oxidation (when the oxide forms on a single side of the sample). Thereafter, the oxidation will always be considered as symmetrical. In Fig. 13, only one side has been drawn for the sake of simplicity;
- Metallic substrate and oxide layer have an elastic + viscoplastic behavior (as usually considered [23]); elasticity is given by Hooke's model: $\sigma = \widetilde{E}\varepsilon^{\mathrm{el}}$; thermal strain is also considered in both materials given by $\varepsilon^{\mathrm{th}} = \alpha\Delta T$;
- Chemical strain due to the dissolution of species within the substrate are possible [24]; within the oxide, there is additional growth phenomena [23];
- The oxide grows uniformly with a parabolic kinetics according to $h_{\mathrm{ox}}(t) = A_{\mathrm{p}}\sqrt{t}$ [14];
- Particles of Ti are assumed to have only an elastic and thermal behavior, without inelasticity;

- Particles oxidation on their top surface (without covering) has no influence on the mechanical balance/state of the system.

Input parameters are the geometry parameters: $L_{\mathrm{m}}$ length of the sample in direction $x$; $L_{\mathrm{p}}$ length of one deposited particle in direction $x$; $h_{\mathrm{ox}}(t)$, $h_{\mathrm{m}}$ and $h_{\mathrm{p}}$ are respectively the thickness of the oxide layer evolving with time due to oxidation, the thickness of metal, and the height of particles. The number of particles in the $x$ direction is also required and will be denoted $N$. It is worth noting that the thickness of the oxide layer evolves with time. When $h_{\mathrm{ox}}(t) \geq h_{\mathrm{p}}$, it is no more possible to obtain information from the gratings because of the covering by oxide grains.

Other input parameters are the materials parameters: $\widetilde{E} = \frac{E}{1-\nu}$ combining Young modulus $E$ and Poisson ratio $\nu$ for in-plane stress state, for oxide, metal and particles. $\alpha$ is the coefficient of thermal expansion for oxide, metal and particles. The kinetics constant $A_{\mathrm{p}}$ is also required. The viscoplastic behavior is presently not necessary to be developed as further explained.

All the numerical data are presented in table 2.

| Properties | Particles [25] | Oxide layer [26], [3] | Metallic substrate [26], [3] |
|---|---|---|---|
| $E$ (GPa) at 800$^o$C | 83.5 | 225 | 170 |
| $\nu$ at 800$^o$C | 0.30 | 0.29 | 0.30 |
| $\widetilde{E}$ (GPa) at 800$^o$C calculated by $\widetilde{E} = \frac{E}{1-\nu}$ | 119.3 | 316.9 | 242.9 |
| $\alpha$ (K$^{-1}$) at 800$^o$C | $12.0 \cdot 10^{-6}$ | $5.67 \cdot 10^{-6}$ | $12.93 \cdot 10^{-6}$ |
| length $L$ (m) | $25 \times 3$ | $10 \cdot 10^3 - 25 \times 3$ | $10 \cdot 10^3$ |
| height $h$ (nm) at 800$^o$C | 300 | $A_{\mathrm{p}}\sqrt{t}$ with $A_{\mathrm{p}} = 2.36 \cdot 10^{-9}\mathrm{m} \cdot \sqrt{\mathrm{s}}$ | $1 \cdot 10^6$ |

Table 2: Numerical values used for analysis of the thermomechanical problem

From the different assumptions, we can get the equations governing the system. The continuity equation related to interface oxide+particles/substrate can be separated during oxidation in the following way for the total strain

$\varepsilon^{\text{tot}}$:

$$\langle \varepsilon^{\text{tot}}_{\text{ox}+p} \rangle = \varepsilon^{\text{tot}}_{\text{ox}} \left(1 - \frac{NL_{\text{p}}}{L_{\text{m}}}\right) + \varepsilon^{\text{tot}}_{\text{p}} \left(\frac{NL_{\text{p}}}{L_{\text{m}}}\right) = \varepsilon^{\text{tot}}_{\text{m}} \tag{7}$$

$$\Leftrightarrow (\varepsilon^{\text{el}}_{\text{ox}} + \varepsilon^{\text{th}}_{\text{ox}} + \varepsilon^{\text{in}}_{\text{ox}}) \left(1 - \frac{NL_{\text{p}}}{L_{\text{m}}}\right) + (\varepsilon^{\text{el}}_{\text{p}} + \varepsilon^{\text{th}}_{\text{p}}) \left(\frac{NL_{\text{p}}}{L_{\text{m}}}\right) = \varepsilon^{\text{el}}_{\text{m}} + \varepsilon^{\text{th}}_{\text{m}} + \varepsilon^{\text{in}}_{\text{m}} \tag{8}$$

where $\langle \varepsilon^{\text{tot}}_{\text{ox}+p} \rangle$ is the average of the total strain for the oxide and particles layer; $\varepsilon^{\text{in}}$ is the inelastic and non-thermal strain, with growth strain and viscoplasticity for oxide layer and chemical strain and viscoplasticity for metal. As assumed, there is no inelastic strain in the particles, i.e. $\varepsilon^{\text{in}}_{\text{p}} = 0$. A mechanical balance is considered between oxide and substrate, such as:

$$\sigma_{\text{ox}} h_{\text{ox}} + \sigma_{\text{m}} h_{\text{m}} = 0 \tag{9}$$

The same kind of relation can be established between particles and substrate.

$$\sigma_{\text{p}} h_{\text{p}} + \sigma_{\text{m}} h_{\text{m}} = 0 \tag{10}$$

Substraction between Eqs. 9 and 10 leads to $\sigma_{\text{p}} h_{\text{p}} = \sigma_{\text{ox}} h_{\text{ox}}$. Due to the mechanical loading developed from growth stress or thermal stress [1, 3], the particles can be interpreted as in serial with the oxide. From these equations, we can solve the problem to find quantities as a function of the particles total strain measured from the gratings, for a given temperature time variation $\Delta T(t)$. Moreover, because the measured strain is different along $x$ and $y$ directions, it is possible to distinguish the three plane components of the different tensors, which will be further denoted by subscripts $jl$. The inelastic and non-thermal strains are unknown. However, the equations are developed such that they do not appear in the final equations, which are:

- Total strain only in the particles (because for oxide and substrate, there is also other strains that we choose to not explicit), given for time $t^k$ from strain mapping of picture $k$ average over all the $N \times N$ particles:

$$\varepsilon^{\text{tot}}_{\text{p},jl}(t^k) = \frac{1}{N^2} \sum_{i=1}^{N^2} \varepsilon^k_{jl}(x_i, y_i) \tag{11}$$

- Stress in the oxide layer, in the metallic substrate and in the particles, for any time:

$$\sigma_{\mathrm{ox},jl}(t) = \widetilde{E}_{\mathrm{ox}} \frac{\frac{\widetilde{E}_{\mathrm{p}}{}^{h}\mathrm{p}}{\widetilde{E}_{\mathrm{ox}}{}^{h}\mathrm{ox}(t)} + \frac{{}^{NL}\mathrm{p}}{{}^{L}\mathrm{m}} \left(1 - \frac{\widetilde{E}_{\mathrm{p}}{}^{h}\mathrm{p}}{\widetilde{E}_{\mathrm{ox}}{}^{h}\mathrm{ox}(t)}\right)}{1 - \frac{{}^{NL}\mathrm{p}}{{}^{L}\mathrm{m}} \left(1 - \frac{\widetilde{E}_{\mathrm{p}}{}^{h}\mathrm{p}}{\widetilde{E}_{\mathrm{ox}}{}^{h}\mathrm{ox}(t)}\right)} (\varepsilon^{\mathrm{tot}}_{\mathrm{p},jl}(t) - \alpha_{\mathrm{p}}\delta_{jl}\Delta T(t)) \tag{12}$$

$$\sigma_{\mathrm{m},jl}(t) = -\frac{\widetilde{E}_{\mathrm{ox}} h_{\mathrm{ox}}(t)}{h_{\mathrm{m}}} \frac{\frac{\widetilde{E}_{\mathrm{p}}{}^{h}\mathrm{p}}{\widetilde{E}_{\mathrm{ox}}{}^{h}\mathrm{ox}(t)} + \frac{{}^{NL}\mathrm{p}}{{}^{L}\mathrm{m}} \left(1 - \frac{\widetilde{E}_{\mathrm{p}}{}^{h}\mathrm{p}}{\widetilde{E}_{\mathrm{ox}}{}^{h}\mathrm{ox}(t)}\right)}{1 - \frac{{}^{NL}\mathrm{p}}{{}^{L}\mathrm{m}} \left(1 - \frac{\widetilde{E}_{\mathrm{p}}{}^{h}\mathrm{p}}{\widetilde{E}_{\mathrm{ox}}{}^{h}\mathrm{ox}(t)}\right)} (\varepsilon^{\mathrm{tot}}_{\mathrm{p},jl}(t) - \alpha_{\mathrm{p}}\delta_{jl}\Delta T(t)) \tag{13}$$

$$\sigma_{\mathrm{p},jl}(t) = \widetilde{E}_{\mathrm{p}}(\varepsilon^{\mathrm{tot}}_{\mathrm{p},jl}(t) - \alpha_{\mathrm{p}}\delta_{jl}\Delta T(t)) \tag{14}$$

  where $\delta_{jl}$ is the Krönecker symbol. Eq. 12 is obtained by use of Hooke's model and by resolution of previous equations to obtain the elastic strain in oxide. Eq. 13 is obtained by use of mechanical balance (Eq. 9) inserting Eq. 12. Eq. 14 is obtained from Hooke's model by partitioning the particles' strain into thermal and elastic ones.

- Elastic strain in the oxide layer, in the metallic substrate and in the particles, for any time, by inverting Hooke's model:

$$\varepsilon^{\mathrm{el}}_{\mathrm{ox},jl}(t) = \widetilde{E}^{-1}_{\mathrm{ox}}\sigma_{\mathrm{ox},jl}(t) \tag{15}$$

$$\varepsilon^{\mathrm{el}}_{\mathrm{m},jl}(t) = \widetilde{E}^{-1}_{\mathrm{m}}\sigma_{\mathrm{m},jl}(t) \tag{16}$$

$$\varepsilon^{\mathrm{el}}_{\mathrm{p},jl}(t) = \widetilde{E}^{-1}_{\mathrm{p}}\sigma_{\mathrm{p},jl}(t) \tag{17}$$

- Thermal strain in the oxide layer, in the metallic substrate and in the particles, for any time:

$$\varepsilon^{\mathrm{th}}_{\mathrm{ox},jl}(t) = \alpha_{\mathrm{ox}}\Delta T(t)\delta_{jl} \tag{18}$$

$$\varepsilon^{\mathrm{th}}_{\mathrm{m},jl}(t) = \alpha_{\mathrm{m}}\Delta T(t)\delta_{jl} \tag{19}$$

$$\varepsilon^{\mathrm{th}}_{\mathrm{p},jl}(t) = \alpha_{\mathrm{p}}\Delta T(t)\delta_{jl} \tag{20}$$

Some quantities can be derived by different ways leading to possible verifications of the calculations.

## 4. Results and data post-treatment

In Fig. 14 is presented the total strain in particles. In Fig. 15, 16, 17 are plotted the different stresses, for particles, for oxide layer and substrate layer respectively. We choose not to present the elastic strain and thermal strain, because it is simply proportional respectively to the stress and to the temperature time variation (given in Fig. 11). The cooling part is not presently presented, because we are mainly interested in the very short times (during heating part), as well as the isothermal part.

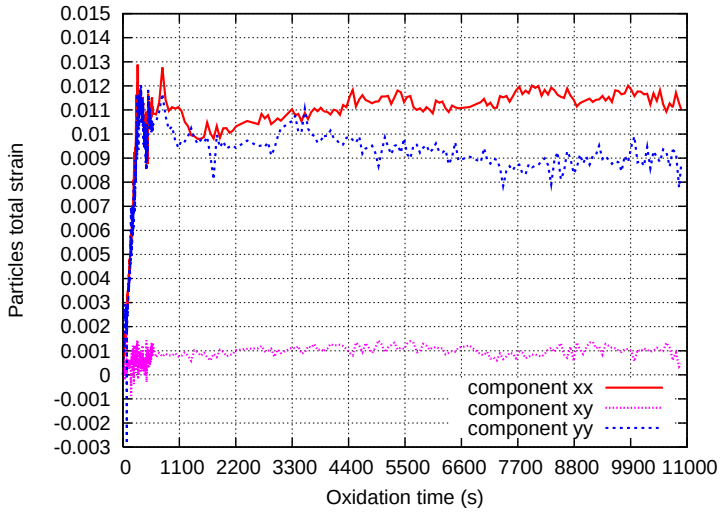


Figure 14: Total strain of particles $\varepsilon_{\mathrm{p}}^{\mathrm{tot}}$ versus time, plotted without the cooling part

The initial strain is zero, whatever the component is. Then a linear variation is observed corresponding to the linear variation of temperature during the heating part. After this part, the particles strain evolves with time until stabilization after 7700s for components $xx$ and $yy$, whereas the component $xy$ is roughly constant just after the heating part. As previously mentioned, the strain does not exceed a maximum of $1.3 \cdot 10^{-2}$.

For the stress, the particles values are in the range $-200$ to 400MPa (see in Fig. 15). The oxide values are in the range $-2.5$ to 2.5GPa (see in Fig. 16), whereas the substrate values are in the range $-120$ to 60Pa (see in Fig. 17). Such an order of values is expected for a metal/oxide system [1, 3]. The ratio of the oxide stress over the substrate stress (around $5 \cdot 10^3$) is due to the ratio of the height of metal (1mm) over the oxide ($\approx 0.25$m).

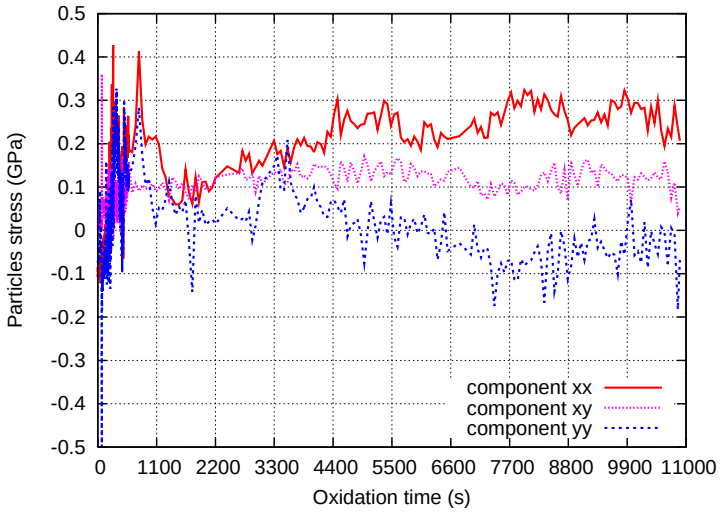


Figure 15: Stress of particles $\sigma_{\mathrm{p}}$ versus time, plotted without the cooling part

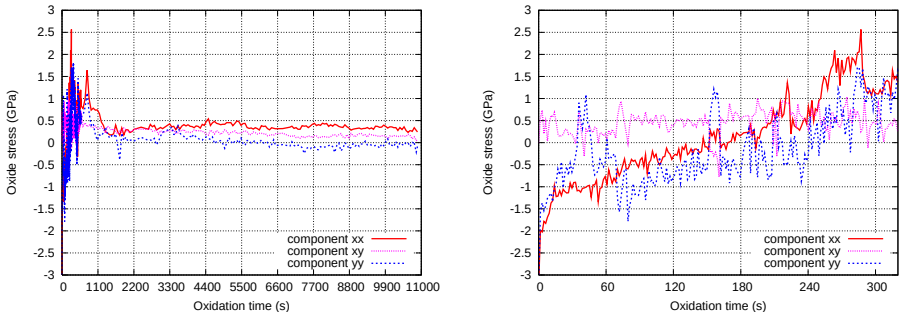


Figure 16: Stress of oxide layer $\sigma_{\mathrm{ox}}$ versus time, plotted without the cooling part; on the left, for all the oxidation time; on the right, magnification of the heating part

Moreover, the same time evolution regimes are identified. A linear evolution is observed during the 310s of the heating part (see Fig. 16 on the right). Then the stresses evolve differently depending on the components and on the phase. This evolution will be further discussed. However, it is important to note that such stresses do not start at zero. It is due to the fact that the reference configuration for strain is considered at 100$^o$C (first saved picture), whereas the reference temperature is at 25$^o$C. Such a choice leads to a systematic error in the stress curves. The evolution is correct, however the exact value for stress is not still correct. A correction of the data is

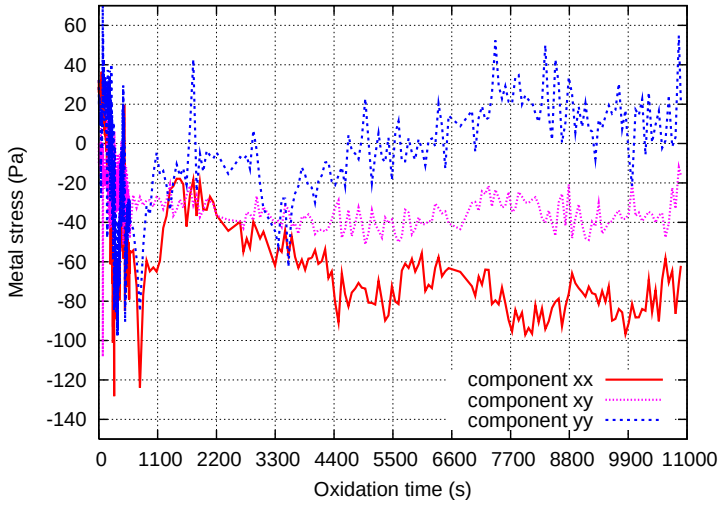


Figure 17: Stress of substrate $\sigma_{\mathrm{m}}$ versus time, plotted without the cooling part

required for deeper investigation during the temperature time variation.

Therefore, the initial stress due to thermal strain can be removed. Indeed, we aim at studying separately the different driving stresses: thermal and growth ones. According to the results, we can assume from linearity of the curves at the beginning (during 310s) that mainly thermal strain occurs. It is also supported by the fact that other strain effects, such as relaxation by viscoplasticity has significant influence only after few hours. Typically, a characteristic time for viscoplasticity was measured in [19] of 1.74h at 800$^o$C. Accordingly, to obtain the stresses only due to growth phenomena during isothermal part, we can thus shift the stress from its value at 310s, for all the oxidation time and for all the components ($\sigma'_{\mathrm{ox},jl}(t) = \sigma_{\mathrm{ox},jl}(t) - \sigma_{\mathrm{ox},jl}(t = 310s)$). For further discussion, we can also translate the time scale from this value ($t' = t - 310\mathrm{s}$). It is presented in Fig. 18.

## 5. Discussion on materials features

From the previous methodology, it has been possible to obtain the stress evolution, especially in the oxide layer as presented in Fig. 18. During the isothermal part, after removing the effect of thermal expansion, we observe

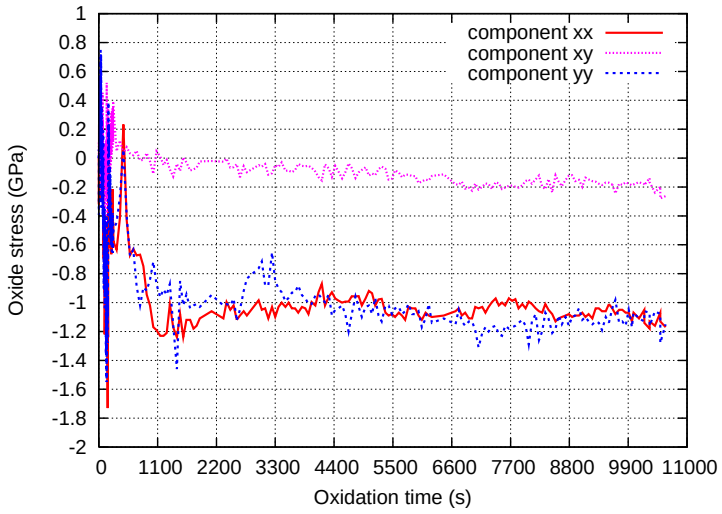


Figure 18: Stress of oxide versus time, plotted without the cooling and heating part, with new zero for time and shifted value for the stress: the coordinates of the first point are $(0, 0)$

that the components of the stress tensor are mainly in compression, as expected for such a system [1, 3].

The shear stress ($xy$ component) has values in the range $-0.5$ to 0.5GPa at the very short times where the measurements present strong oscillations. After, we observe that the shear stress is roughly zero at the beginning time (above 2200s) and slightly decreases after at the scale of measurements. Nevertheless, the values are small compared to the ones for the two other components.

Indeed, for the components $xx$ and $yy$, values around up to $-1.3$GPa are observed. It is worth noting that both components present similar values and trends, meaning that the system presents an isotropic mechanical state for all oxidation time. The assumption for a 2D problem is thus validated and confirmed that the present geometry and distribution/pattern of Ti particles do not modify the mechanical state commonly assumed [27]. The evolution of stress with time presents three main parts. First, the stress decreases up to an important values as previously mentioned. Then relaxation occurs with an inflexion time around 1200s. Therefore stress tends slightly to increase (which is more pronounced for the $xx$ component). After 5500s, the level of

stress is roughly constant around $-1.1$GPa.

A similar evolution was identified in [19] at 800$^o$C on Ni30Cr oxidized during 7.5h by use of in-situ Raman spectroscopy, with the same trends and almost the same values (maximum at inflexion time of $-1.5$GPa and constant value at long times of $-0.75$GPa). The main difference was on the inflexion time value found approximately around 7500s.

Because of the obtained values, the assumptions concerning the influence of a growing oxide at the particle/substrate interface can be discussed. With an oxide interphase of bigger Young modulus than the particle (see in Table 2), the data treatment would lead to a higher value of stress, in absolute value, in the oxide layer, according to Eq. 12. It would not be consistent with the literature values for this system. The oxidation of the system for higher oxidation times has shown the covering of the gratings that goes in the same way, which is also the main drawback of the method.

The evolution of the oxide stress is also quite consistent with the theoretical interpretation of the growth phenomena in such a system [23]. Indeed, from this curve of stress evolution, it is possible to analyze some features of the material. At the short oxidation times, some modeling proposes that the driven force for oxide stress evolution is related to the oxide thickness evolution, as for example in the Clarke's model [27]. A material coefficient $D_{\mathrm{ox}}$ is introduced that can be interpreted differently. It can be related to microstructural mechanisms especially diffusion, then oxidation within the oxide layers along vertical grain boundaries [27]. Another interpretation of this mechanism was proposed from a transition scale approach in a thermodynamic framework in [23].

It is particularly interesting to determine numerical values for such a material parameter. It has been performed in [26] by comparison of a full mechanical modelling with different experimental methods. However, none of them concerns the present method using micro/nano-gauges. In such a work, it is proposed to relate for short oxidation times the oxide stress with time as:

$$\sigma_{\mathrm{ox}}(t) \approx -\frac{D_{\mathrm{ox}}E_{\mathrm{ox}}A_{\mathrm{P}}}{1-\nu_{\mathrm{ox}}}\sqrt{t-t_0} \tag{21}$$

$$\Leftrightarrow \sigma^2_{\mathrm{ox}}(t) \approx \left(\frac{D_{\mathrm{ox}}E_{\mathrm{ox}}A_{\mathrm{P}}}{1-\nu_{\mathrm{ox}}}\right)^2 (t-t_0) \tag{22}$$

where $t_0$ is the initial time of the data, chosen here equal to zero because of the time shift of data as previously explained. We can then fit the first part of

the Fig. 18 (before the inflexion time around 1200s and by removing aberrant points) by use of Eq. 22, for a constraint intercept at zero. It leads to the slope of $1.2 \cdot 10^{-3}\text{GPa}^2/\text{s}$ with a statistical uncertainty of $7.23 \cdot 10^{-5}\text{GPa}^2/\text{s}$. By use of numerical values given in Table 2, we can then calculate the value for $D_{\text{OX}}$ that is $4.63 \cdot 10^4 \pm 1.14 \cdot 10^4 \text{m}^{-1}$. This method of calculation is strongly dependent on the value of the oxidation kinetics. The value for $D_{\text{OX}}$ is nevertheless comparable to those given in [26], between $10^3$ and $1.5 \cdot 10^4 \text{m}^{-1}$, especially for similar values of the oxidation kinetics.

It is also interesting to emphasize that the inverse of this quantity is homogeneous to a length that can be related to the microstructure as interpreted in [23] as a lateral length at a scale greater than the oxide grain size. In the present case, this length is calculated as $L^I \approx D_{\text{OX}}^{-1} = 21.6 \pm 5.6\text{m}$, showing that it is related to a microstructural component. Typically, this value is bigger than the oxide grain size (smaller than the oxide thickness of 250nm at $800^o$C), but similar to the metal grain size as presently determined by EBSD (average around 25m). In such a case, we may then interpreted the average grain size of metal as the minimum length scale to define the growth strain by use of Clarke model for use in mechanical balance between metal and oxide. However, it should be emphasized that the lateral size of gauges (3m) may also influence the growth mechanism: measure could perturb the growth phenomena. It is thus difficult to conclude about this length. In addition, it is necessary to apply the present method to other materials to confirm this trend and improve its reliability.

## 6. Conclusions

In the present work, we have developed a quantitative and complex method to obtain mechanical information in metal/oxide systems.

It is based on the fabrication of innovative coatings in clean room to obtain gauges for the present goal: in-situ following during high-temperature oxidation. Typically, by comparison between different materials, we have been able to build gratings of particles adapted for in-situ following of surface mechanical state during high temperature oxidation. Because of different constraints during fabrication and use, the particles are both namometric and micrometric. Further developments are required to optimize the geometry and increase the accuracy of the method. Moreover, other materials or assembly of materials are in development especially to increase the efficiency with

a better contrast, as well as the limit of temperature for high-temperature environments.

The method is based on data treatment of displacement of particles of gratings. Then the calculated strain of particles leads to the stress in the different phases. Several assumptions are required to obtain the different quantities. Even adapted for the present configuration, some of them need still to be investigated to test the limits of the method. An interesting possibility would be to compare with the particles strain by use of the evolution of their radius.

Nevertheless, the method has been successfully applied to a Ni38Cr metallic substrate oxidized at $800^o$C for 3 hours. The method is especially interesting for short oxidation times when the kinetics of stress evolves quickly. During 3 hours, the particles of the gratings are still visible without significant problem of covering. After removing the effect of thermal expansion, it is possible to obtain the stress especially due to growth during isothermal loading due to oxidation. The time evolution of stresses components has been successfully obtained with similar variations as obtained with Raman spectroscopy. The oxide stress is confirmed to be in compression with high amplitude (around $-1.1$GPa) with growth effect as well as relaxation part. The method has also applied to determine the growth parameter involved in stress evolution for short oxidation times. The numerical value presently obtained is in agreement with previous values and enables an interpretation of this parameter in relation to the microstructure. The method is proved to be adapted for the determination of thermomechanical behavior in high temperature oxidation.

*Acknowledgements.* This work has been supported by the EIPHI Graduate School (contract "ANR-17-EURE-0002") and by the Agence Nationale de la Recherche and the FEDER (INSOMNIA project, contract "ANR-18-CE09-0003"). Financial support of NanoMat (www.nanomat.eu) by the "Ministère de l'enseignement supérieur et de la recherche," the "Conseil régional Champagne-Ardenne," the "Fonds Européen de Développement Régional (FEDER) fund", and the "Conseil général de l'Aube" is also acknowledged. The authors also thanks the M2P IRT support for funding the COMODO and COMBINE RESEM projects.

[1] M. Schütze, Protective oxide scales and their breakdown, Wiley, 1991.

[2] P. Kofstadt, High temperature corrosion, Elsevier, Applied Science Publishers, England, 1998.

[3] A.M. Huntz, B. Pieraggi, Oxydation des matériaux métalliques, Hermès Science, Paris, 2003.

[4] B. Panicaud, J.L. Grosseau-Poussard, P. Girault, J.F. Dinhut, D. Thiaudière, Comparison of growth stress measurements with modelling in thin iron oxide films. Appl. Surf. Sci. 252 (2005) 5700-5713.

[5] A.M. Huntz, G. Calvarin-Amiri, H.E. Evans, G. Cailletaud, Comparison of oxidation-growth stresses in NiO film measured by deflection and calculated using creep analysis or Finite-Element modeling. Oxid. Met. 57 (2002) 499-521.

[6] J. Marae Djouda, G. Montay, B. Panicaud, J. Béal, Y. Madi, T. Maurer, Nanogauges gratings for strain determination at nanoscale. Mechanics of Materials 114 (2017) 168-178.

[7] J. Marae Djouda, Y. Madi, F. Gaslain, J. Beal, J. Crépin, G. Montay, L. Le Joncour, N. Recho, B. Panicaud, T. Maurer, Investigation of nanoscale strains at the austenitic stainless steel 316L surface: Coupling between nanogauges gratings and EBSD technique during in situ tensile test. Mater. Sci. Eng. A 740-741 (2019) 315-335.

[8] J. Marae Djouda, B. Panicaud, F. Gaslain, J. Béal, G. Montay, L. Le Joncour, J. Gardan, N. Recho, J. Crépin, T. Maurer, Local microstructural characterization of an aged UR45N rolled steel: Application of the nanogauges grating coupled EBSD technique. Mater. Sci. Eng. A 759 (2019) 537-551.

[9] A. Clair, M. Foucault, O. Calonne, Y. Lacroute, L. Markey, M. Salazar, V. Vignal, E. Finot, Strain mapping near a triple junction in strained Ni-based alloy using EBSD and biaxial nanogauges. Acta Mater. 59 (2011) 3116-3123.

[10] S.C. Tsaï, A.M. Huntz, C. Dolin, Diffusion of $^{18}O$ in massive $Cr_2O_3$ and in $Cr_2O_3$ scales at $900^oC$ and its relation to the oxidation kinetics of chromia forming alloys. Oxid. Met. 43 (1995) 581-596.

[11] S.C. Tsaï, A.M. Huntz, C. Dolin, Growth mechanism of $Cr_2O_3$ scales: oxygen and chromium diffusion, oxidation kinetics and effect of yttrium. Mater. Sci. Eng. A 212 (1996) 6-13.

[12] R.J. Hussey, M.J. Graham, The influence of reactive-element coatings on the high-temperature oxidation of pure-Cr and high-Cr-content alloys. Oxid. Met. 45 (1996) 349-374.

[13] S.C. Tsaï, A.M. Huntz, J. Philibert, Diffusion of $^{54}Cr$ and $^{18}O$ in $Cr_2O_3$ scales and growth mechanism. Defects and Diffusion Forum 143-147 (1997) 1195-1200.

[14] M. Guerain, F. Rakotovao, S.Y. Brou, G. Bonnet, B. Panicaud, J.L. Grosseau-Poussard, P. Goudeau, Stress release in $\alpha$-$Cr_2O_3$ oxide thin films formed on Ni30-Cr and Fe47-Cr alloys. Journal of Alloys and Coumpounds 718 (2017) 223-230.

[15] P. Moulin, A.M. Huntz, P. Lacombe, Influence des phénomènes diffusionnels sur le mécanisme d'oxydation des alliages Ni-Cr. Acta Metall. 28 (1980) 745-756.

[16] B. Panicaud, J.L. Grosseau-Poussard, M. Kemdehoundja, J.F. Dinhut, Mechanical features optimization for $\alpha$-$Cr_2O_3$ oxide films growing on alloy NiCr30. Comp. Mat. Sci. 46 (2009) 42-48.

[17] J. Mougin, PhD Thesis, Université de Grenoble, 2001.

[18] L. Bataillou, C. Desgranges, L. Martinelli, D. Monceau, Modelling of the effect of grain boundary diffusion on the oxidation of Ni-Cr alloys at high temperature. Corrosion Science 136 (2018) 148-160.

[19] M. Kemdehoundja, J.F. Dinhut, J.L. Grosseau-Poussard, M. Jeannin, High temperature oxidation of Ni70Cr30 alloy : determination of oxidation kinetics and stress evolution in chromia layers by Raman spectroscopy. Mater. Sci. Eng. A 435-436 (2006) 666-671.

[20] F. Rakotovao, B. Panicaud, J.L. Grosseau-Poussard, Z. Tao, G. Geandier, P.O. Renault, G. Bonnet, P. Girault, P. Goudeau, N. Boudet, N. Blanc, Viscoplastic characteristics of thermally grown chromia films obtained from in situ 2D synchrotron X-ray diffraction. Journal of Alloys and Compounds 744 (2018) 591-599.

[21] D.H. Ballard, Generalizing the Hough Transform to Detect Arbitrary Shapes. Pattern Recognition 13-2 (1981) 111-122.

[22] S. Nemat-Nasser, Plasticity - A Treatise On Finite Deformation of Heterogeneous Inelastic Materials, Cambridge University Press, 2004.

[23] B. Panicaud, J.L. Grosseau-Poussard, J.F. Dinhut, General approach on the growth strain versus viscoplastic relaxation during oxidation of metals. Comp. Mat. Sci. 42 (2008) 286-294.

[24] J. Favergeon, T. Montesin, G. Bertrand, Mechano-Chemical Aspects of High Temperature Oxidation: A Mesoscopic Model Applied to Zirconium Alloys. Oxid. Met. 64 (2005) 253-279.

[25] S. Nemat-Nasser, W.G. Guo, J.Y. Cheng, Mechanical properties and deformation mechanisms of a commercially pure titanium. Acta Mater. 47-1 (1999) 3705-3720.

[26] J.L. Grosseau-Poussard, B. Panicaud, S. Ben Afia, Modelling of stresses evolution in growing thermal oxides on metals. A methodology to identify the corresponding mechanical parameters. Comp. Mat. Sci. 71 (2013) 47-55.

[27] D.R. Clarke, The lateral growth strain accompanying the formation of a thermally grown oxide. Acta Mater. 51 (2003) 1393-1407.